

Geometric calibration and image rectification of a multi-line scan camera for accurate 3D reconstruction

Bernhard Blaschitz, Svorad Štolc, Doris Antensteiner; AIT Austrian Institute of Technology; Vienna, Austria

Abstract

Multi-line scan systems have been introduced as linear light field cameras and subsequently for 3D ranging for industrial in-line applications. Up to now there have been no viable calibration methods to determine intrinsic and extrinsic parameters of such a system which would allow (i) metric measurements and (ii) line-scan image geometric rectification. Our work closes the gap by exploiting special properties of a typical multi-line scan setup, which internally uses a fast area-scan sensor that can also be operated in the line-scan mode. This allows the use of standard calibration approaches to determine the intrinsic camera parameters. We introduce a novel method to compute extrinsic camera parameters w.r.t. the transport direction. Consecutively, the images are rectified for all constructed line-scan views. This takes into account estimated camera model parameters in order to generate an EPI-corrected linear light field that is suitable for accurate 3D reconstructions. Furthermore, we introduce a novel calibration target that is characteristic by an asymmetric central element as well as a tailored fast detection algorithm. The proposed method significantly improves the 3D reconstruction quality and allows for absolute 3D measurements in metric units using the multi-line scan setup. The performance of the proposed method is demonstrated on several representative real world examples.

Introduction

For light field processing in inline applications, where objects are inspected while moving on a linear transport stage, multi-line scan cameras are highly suited due to fast acquisition and processing speeds. In our previous work we introduced algorithms for multi-line scan cameras for a precise 3D reconstruction via multi-view stereo [15] and hybrid approach exploiting additional photometric stereo cue for improved depth detail [1].

So far multi-line scan setups were deployed only with high quality industrial lenses with little to no optical distortions and at resolutions where mechanical adjustments was sufficient. However, when used with lenses with more geometrical distortion, lower quality lenses, at higher resolutions or with imprecise adjustment, a geometrical calibration became essential to achieve accurate 3D measurements. We present an approach to find a new virtual sensor plane oriented such that the linear transport is taken into account. Our method allows a significantly improved 3D reconstruction results.

Numerous geometric calibration targets are commercially available (e.g. [6]), however for high accuracy / high magnification measurement a target with very low manufacturing tolerances (in μm -range) is required. This requirement essentially excludes all targets printed on a standard office printer. Additionally, due to a small field of view at high magnifications the appropriate calibration target needs to contain a small easy-to-recognize marker

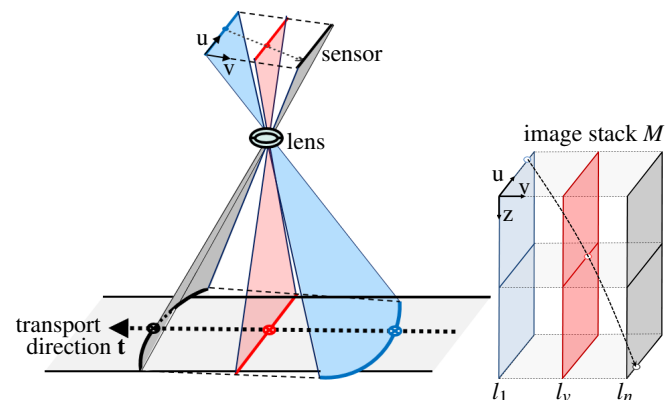


Figure 1: Illustration of a multi-line scan acquisition setup (left) that includes lens distortion as well as rotation w.r.t. the transport. At each time instance a set of lines is captured from the sensor, then the object is moved by a constant increment. Each line captures the object under a different viewing angle and is subject to a different perspective transform and lens distortion. All constructed views are saved in an image stack (right). Note that, with an uncalibrated system, object points may travel along bent curves within the image stack. Each horizontal slice through the image stack represents one multi-line frame captured by the sensor at a single time instance.

in the center, as there is no guarantee to see the whole pattern. Hence, our approach was to take a high-precision grid distortion target from a well-established manufacturer and design and apply our own central marker. For our very small asymmetric marker we also developed a fast and reliable detection method.

Related work

There exist numerous toolboxes for the geometric calibration of area-scan cameras. Although the multi-line scan camera is usually built around a fast area-scan sensor, which is operated in a multi-line scan mode that is capable of capturing multiple line-scan images simultaneously. This is a very specific line-scan setup in which standard calibration methods such as [2, 13] can be used to compute intrinsic camera parameters including a lens distortion model. Extrinsic parameters need to be estimated and interpreted in a system-specific way w.r.t. the direction of the transport stage. To our knowledge, there has not been a practical method to rectify multi-line scan data for 3D reconstruction tasks. Therefore, we propose a novel rectification procedure as well as provide method for calibrated 3D reconstruction using rectified image stacks.

Line-scan calibration usually either uses (i) structured light [11], (ii) originates in remote sensing and assumes the transport

direction to be orthogonal to the line scan direction [3, 7, 8, 9], (iii) assumes an orthogonal transport condition [5, 12], and finally (iv) systems that consist of a camera and a 2D laser finder [16].

Calibrating the multi-line scan camera

The image stack $M \in \mathbb{R}^{m \times n \times p}$ for our multi-line scan setup consists of n images corresponding to the sensor lines l_1, \dots, l_n read from the camera (see Fig. 1). Due to the nature of our setup, the distortion of image v is constant along the z -axis, namely the lens distortion's segment of l_v because of the constant transport. Furthermore, since transport direction $\mathbf{t} = (t_1, t_2, t_3)$ and sensor plane \mathbf{I} can be in arbitrary position w.r.t. each other, there will almost certainly be a perspective warping from line l_v to l_{v+1} (e.g. shearing).

In the following we will describe an algorithm for mapping from each line's pixel positions \mathbf{x} to new positions \mathbf{x}^{new} that corrects these lens distortions and perspective warpings along sensor lines.

Calibration parameters and transport direction

The multi-line scan camera uses a single optical system (see Fig. 1) and can operate also as an area-scan camera. Hence, we acquire images of a planar calibration target and compute all intrinsic and extrinsic camera parameters, that include focal length f , principal point \mathbf{c} and distortion vector \mathbf{k} , using a conventional area-scan calibration approach [2, 13]. We assume that the world coordinates origin in the camera center \mathbf{O} and that the third coordinate axis $\mathbf{w} = (0, 0, 1)$ coincides with the principal ray. Therefore, the image plane (or sensor plane) \mathbf{I} is spanned by vectors $\mathbf{u} = (1, 0, 0)$ and $\mathbf{v} = (0, 1, 0)$ and centered at $\mathbf{c} = (0, 0, f)$.

It is important to use the linear transport stage for a subset of these images, so that we also get a good estimate of the normalized transport direction \mathbf{t} w.r.t. the camera-centered world coordinate system. For a high-precision linear stage, the distances of the calibration target in a series of acquisitions is known (up to a tolerance provided by the manufacturer) and can be used to evaluate the accuracy of the calibration method in metric units.

Virtual image sensor plane

We reconstruct a rectified image stack obtained the multi-line scan camera by defining a new virtual image plane \mathbf{I}' and warping the original line scan images accordingly. Hence, we define a new coordinate system:

$$\begin{aligned} \mathbf{u}' &= 1/\sqrt{t_1^2 + t_2^2} \cdot (t_2, -t_1, 0) \\ \mathbf{v}' &= (t_1, t_2, t_3) \\ \mathbf{w}' &= 1/\sqrt{t_1^2 + t_2^2} \cdot (-t_1 t_3, -t_2 t_3, t_1^2 + t_2^2), \end{aligned} \quad (1)$$

as illustrated in Fig. 2. The vectors \mathbf{u}' and \mathbf{v}' span a new sensor plane \mathbf{I}' , which has the following properties:

- its center $\mathbf{c}' = f \cdot \mathbf{w}'$ has distance f to the camera's center, i.e. the distance from the camera centers to the image planes is the same, so there is minimum scaling from \mathbf{I} to \mathbf{I}' ,
- the \mathbf{v}' -axis is aligned with the transport direction \mathbf{t} , hence image points only move along one axis, which is equivalent to the stereo vision EPI-constraint which makes stereo correspondence analysis a 1D problem, and

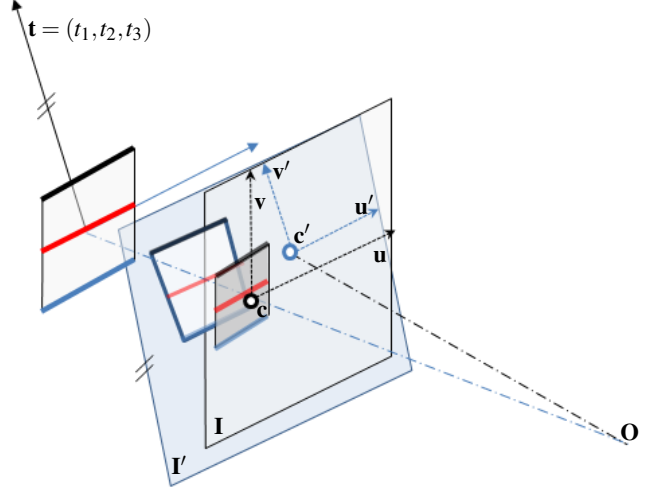


Figure 2: In the classical pinhole model (ignoring lens distortion), an object in space (abstracted as three colored lines) is mapped onto the image plane \mathbf{I} with the principal point \mathbf{c} at its center at distance f from the camera center. We propose a new image plane \mathbf{I}' also at distance f which has the \mathbf{v}' -axis parallel to the transport direction \mathbf{t} . A homography H maps from one coordinate system to the other.

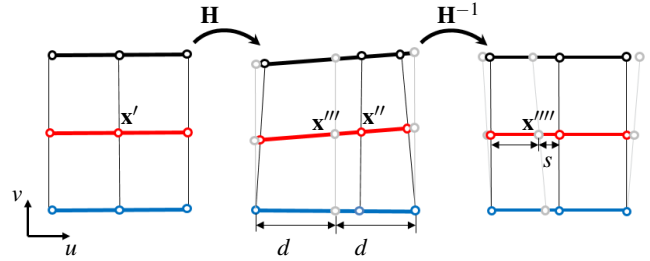


Figure 3: The images of three parallel lines in the old sensor plane \mathbf{I} when taking lens distortion into account are called \mathbf{x}' (left). Their perspectively warped projections \mathbf{x}'' onto \mathbf{I}' are resampled as \mathbf{x}''' such that their distances in u' -direction are equal (middle). We then project back into the original sensor plane \mathbf{I} (right).

- the rotation from \mathbf{w} to \mathbf{w}' around the camera's center is minimal, thus the perspective distortions from images in \mathbf{I} to images in \mathbf{I}' are minimal.

Pixel warping algorithm

In this section we introduce algorithmic details of our pixel warping procedure.

1. Shift & undistort. To rectify the line scan images, each pixel position on the sensor $\mathbf{x} = (u, v)$, where $u = \{1, \dots, m\}$ iterates over all the pixels of one line and $v = \{1, \dots, n\}$ over the line indices, is translated such that the principal point \mathbf{c} is at $(0, 0)$ and undistorted according to focal length f and the distortion vector \mathbf{k} . The new positions are denoted as $\mathbf{x}' = (x', y')$.

2. Project to virtual sensor. Each homogenized pixel position $(x', y', 1)$ is projected onto the new image plane through the

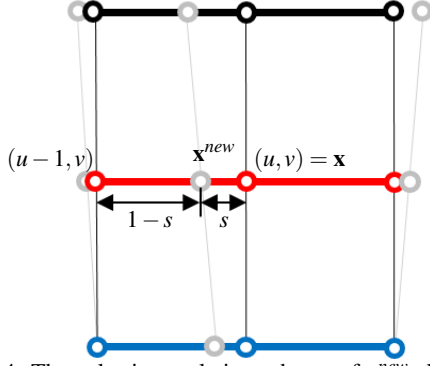


Figure 4: The color interpolation scheme of \mathbf{x}^{new} along line l_v is derived from the linear interpolation between the back projections \mathbf{x}^{new} onto \mathbf{I} and the original positions $(u-1, v)$ and (u, v) .

camera center by a homography in projective 3-space:

$$\mathbf{H} = \begin{pmatrix} u'_1 & v'_1 & w'_1/f \\ u'_2 & v'_2 & w'_2/f \\ fu'_3 & fv'_3 & w'_3 \end{pmatrix} \quad (2)$$

$$= \begin{pmatrix} 1 & & \\ & 1 & \\ & & f \end{pmatrix} \cdot \mathbf{U} \cdot \begin{pmatrix} 1 & & \\ & 1 & \\ & & 1/f \end{pmatrix},$$

$$\text{with } \mathbf{U} = \begin{pmatrix} u'_1 & v'_1 & w'_1 \\ u'_2 & v'_2 & w'_2 \\ u'_3 & v'_3 & w'_3 \end{pmatrix} \text{ and } \mathbf{U}^{-1} = \mathbf{U}^T.$$

Hence a point $\mathbf{x}' \in \mathbf{I}$ is mapped to $\mathbf{x}'' = f/(x'u'_1 + y'u'_2 + f w'_3) \cdot (x'u'_1 + y'u'_2 + f w'_3, x'v'_1 + y'v'_2 + f v'_3) \in \mathbf{I}'$. The mapping of sensor lines under \mathbf{H} is visualized in Fig. 3 as the transformation between the *left* and *center* image.

3. Resample. We resample such that the u' -coordinates are evenly spread between their smallest and their biggest value and the v' -coordinate is linearly interpolated. The new coordinates are denoted as \mathbf{x}''' . This corresponds to the *central* image in Fig. 3.

4. Project back. The resampled coordinates are projected back onto \mathbf{I} by the inverse of Eq. 2

$$\begin{aligned} \mathbf{H}^{-1} &= \text{diag}(1, 1, f) \cdot \mathbf{U}^T \cdot \text{diag}(1, 1, 1/f) \\ &= \begin{pmatrix} u'_1 & u'_2 & u'_3/f \\ v'_1 & v'_2 & v'_3/f \\ fw'_1 & fw'_2 & w'_3 \end{pmatrix}, \end{aligned} \quad (3)$$

and we call $\mathbf{x}'''' = f/(x'''u'_1 + y'''v'_1 + f w'_1, x'''u'_2 + y'''v'_2 + f w'_2) \in \mathbf{I}$.

5. Distort & unshift. Finally, we distort the pixel positions according to our camera and distortion model to arrive at \mathbf{x}^{new} .

Rectification of the image stack

To allow for simpler and faster correspondence analysis one needs to use the estimated calibration parameters in order to get the EPI-corrected image stack. The mapping from \mathbf{x} to \mathbf{x}^{new} is constant with respect to the v - and z - component, hence only the u -component of the pixel positions changes along a line l_v . Our input image stack has color values $M(u, v, z)$ and these do not change under the distortion and the coordinate transforms \mathbf{H} , thus $M(\mathbf{x}) = M(\mathbf{x}') = M(\mathbf{x}'')$. The color values $M(\mathbf{x}^{new}) = M(\mathbf{x}''') =$

$M(\mathbf{x}''')$ are interpolated linearly in the new sensor plane \mathbf{I}' as

$$M(\mathbf{x}''', v) = s \cdot M(u, v) + (1-s) \cdot M(u-1, v), \quad (4)$$

where $s = \mathbf{x}^{new} - \mathbf{x} = x^{new} - u \in \mathbb{R}$ (see Fig. 4 for the geometric interpretation).

To rectify the line-scan image with index v , we duplicate (x_i^{new}, v) with $i = \{1, \dots, m\}$ for all p frames of the image. This $m \times p$ map tells us how to interpolate each pixel. For all n views we get $m \times n \times p$ maps which transform the old image stack to its rectified version (see Fig. 5).

New 3-dot calibration target

In order to facilitate better quality calibration with fewer acquisitions of the calibration target, especially at high magnifications, we have developed a new central marker consisting of three asymmetric dots printed on an off-the-shelf high precision regular dot pattern calibration target (see Fig. 6).

The main advantage of a calibration target with such a central element is that its markers may fill the entire field of view of the camera as long as the central element is readable (cf. [6]). Moreover, our new central marker is designed to be robust and easy to recognize while providing information about image mirroring. We claim that due to the 3-point central element, it is one of the smallest possible asymmetric configurations.

Algorithm for pattern detection

The new calibration target comes with an algorithm for the detection that proceeds as follows:

1. Detect & filter. Acquire area-scan images, identify circular blobs B_k , filter them by circularity and average size according to predefined thresholds and put them into the list of all blobs \mathbf{A} .

2. Sort by diameter. Compare each blob's diameter to the average diameter of four of its direct neighbors and sort the list according to this ratio, resulting in a list of sorted blobs \mathbf{B} .

3. Detect potential central elements. Starting with the biggest element of this list, e.g. $B_k \in \mathbf{B}$, check if exactly two of B_k 's 24 nearest neighbors B_k^+, B_k^- are also in \mathbf{B} . If so, copy $C_k := B_k$ into a new list of possible central elements $\mathbf{C} \subset \mathbf{B}$. Continue for some or all members of \mathbf{B} .

4. Find optimal transform. For each of these $C_k \in \mathbf{C}$, check all 6 possible affine transformations T_j that map C_k and its neighbors C_k^+, C_k^- to their ideal versions i, i^+, i^- of the grid \mathbf{G} (see Fig. 6), i.e.

$$\begin{aligned} T_1(C_k) &= i, \quad T_1(C_k^+) = i^+, \quad T_1(C_k^-) = i^- \\ &\vdots \quad \text{etc.} \\ T_6(C_k) &= i, \quad T_6(C_k^+) = i^+, \quad T_6(C_k^-) = i^- \end{aligned} \quad (5)$$

and map all other blobs $B_k \in \mathbf{A}$ by T_j . Take the central element $\{C_k, C_k^+, C_k^-\}$ and the transform T_c for which the distance of 8 nearest neighbors of i under T_c from the grid is minimal and below a threshold.

5. Begin gridding. Knowing that $T_c(C) = i$, map i 's 1-ring (8-connected neighborhood) j into the grid using T_c and take the nearest $B_k \in \mathbf{A}$ for which $\|T_c(B_k) - \{i_1, \dots, i_8\}\|$ is smaller than some threshold. This assigns 2-dimensional grid coordinate to each discovered B_k (the 8 orange points surrounding i in Fig. 7).



Figure 5: Left- and right-most (out of several) light field images obtained by the multi-line scan camera: before (top) and after (bottom) application of the proposed geometric calibration. The auxiliary grid of green lines shows how each pixel compares from left to right, the auxiliary red lines emphasize lens distortion in the uncalibrated views. Note that this method only rectifies in the vertical direction and that horizontal EPI shifts using y''' have to be taken into account during the 3D reconstruction.

6. Dilate gridded area. Check if there is a square formation of already discovered grid points that has not been explored yet (the gray box containing j in Fig. 7, right), if so, update the transform to T_{next} using these four points and search for the nearest B_k as in step (5). Otherwise, search for a new unexplored square formation defined by point j .

Note that this gridding mechanism can be applied also when some points in the grid are undetected.

7. Finish. Keep track of all visited points in the grid \mathbf{G} as well as their corresponding coordinates in the input image.

Once no new B_k are found for all possible choices of j , end the algorithm.

The proposed gridding algorithm can be implemented very efficiently using intelligent caching strategy which avoids use recursion in the search for new grid points. Therefore our prototype implementation showed performance already superior to other available solutions. Thanks to circular grid points, our calibration target also proved to be suitable for systems with shallow depth of field, as circular blobs can be detected quite robustly even if they are out of focus. Moreover, their centroids are not too affected by the defocus which contributes to good accuracy of the final calibration model obtained using such a target.

Calibrated 3D reconstruction

Once the calibration parameters are known for a given multi-line scan setup and the image stack is EPI-rectified accordingly, a multi-view correspondence analysis is carried out making use of depth hypothesis testing (see e.g. [15]). For a calibrated system and each tested depth hypothesis z_i (in metric units) there exists a matrix $D_i(u, v) \in \mathbb{R}^{m \times n}$ that carries all associated disparities for

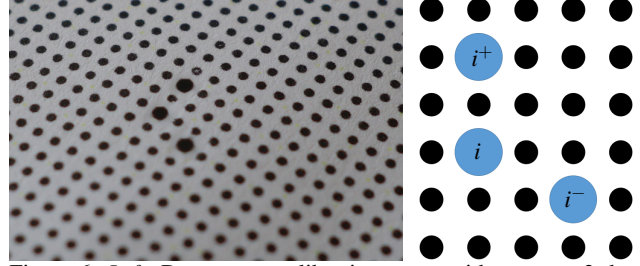


Figure 6: *Left*: Dot pattern calibration target with our new 3-dot central element. *Right*: Abstract description of the pattern. Note that this pattern is the smallest possible asymmetric configuration on a regular grid and three distinct marks suffice to estimate an affine transformation, which approximates the more general perspective transformation needed to unwarp the image.

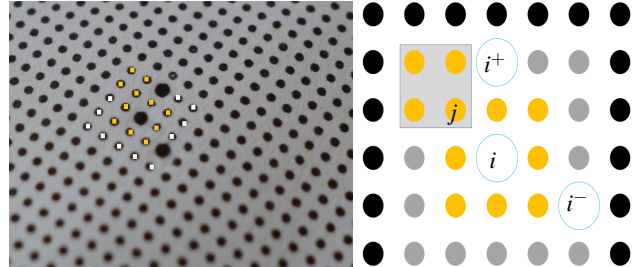


Figure 7: *Left*: Original image with detected grid points. *Right*: Gridding strategy of grid \mathbf{G} .

each line u and view v

$$D_i(u, v) = \frac{y'''(u, v)}{f} \cdot \frac{z_i}{T_{step}}, \quad \forall u, v, \quad (6)$$

where f and y''' come as the result of our calibration procedure described earlier and T_{step} is the transport increment (in metric units) given by the transport control. Afterwards, the obtained disparity matrix D_i is used to steer the correspondence analysis in order to test a number of depth hypotheses z_i . The multi-view correspondence analysis itself as well as the rest of the 3D reconstruction pipeline may be implemented via standard state-of-the-art algorithms such as [4, 10, 14]. Finally, this turns the multi-line scan system into a measurement device.

It should be noted that, unlike standard area-scan stereo systems with fixed baseline and therefore fixed z -resolution, the multi-line scan camera offers a flexibility in choosing baseline depending on the required depth sensitivity. It can be shown that the z -resolution (in metric units) of the multi-line scan camera is defined as

$$z_{res} = \frac{f}{\max(y''') - \min(y''')} \cdot T_{step}. \quad (7)$$

It follows z_{res} is directly proportional to the transport increment T_{step} (i.e. speed), which is a parameter that can be defined adaptively by the user without necessity of any hardware change. E.g. if high depth detail is required for the given application a lower acquisition speed need to be applied, while if only low detail is sufficient the system may acquire adequately faster. That is indeed an important advantage over other depth sensing methods with fixed depth resolution.

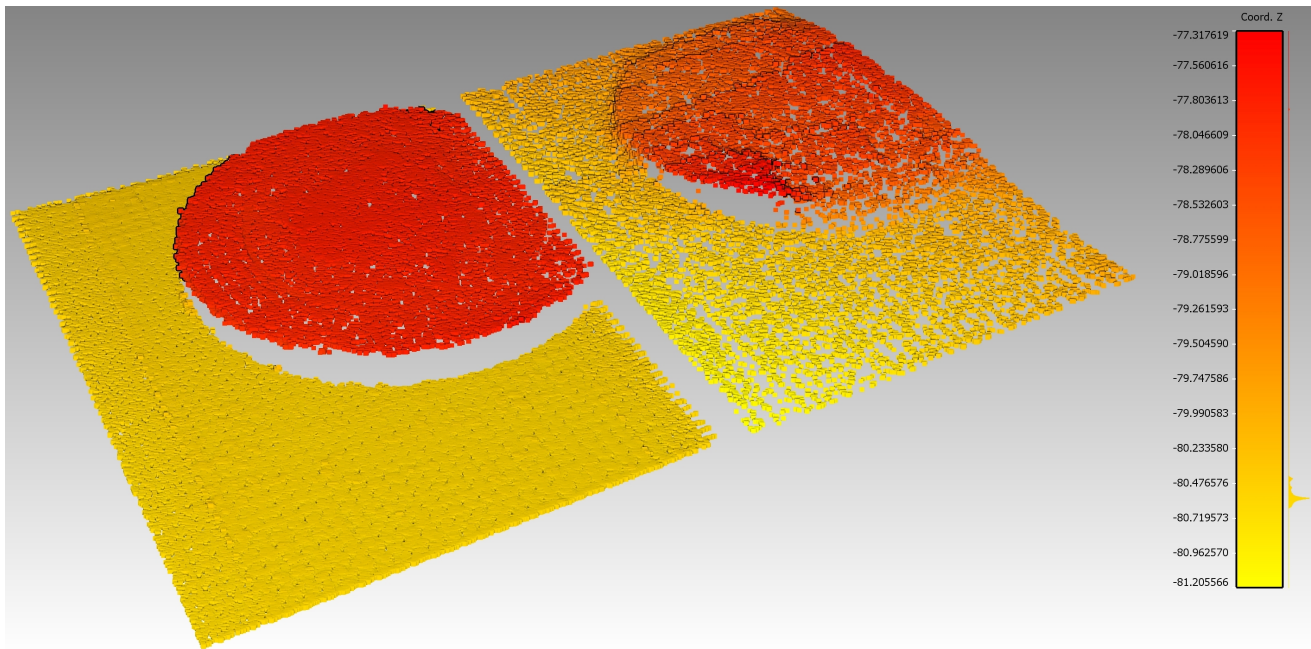


Figure 8: 3D reconstruction of the image stack shown in Fig. 5 for calibrated (*left*) and uncalibrated (*right*) system. Presented 3D models use pseudo-coloring according to the distance from the camera center.

Experimental results

Several illustrative examples of reconstructed 3D point clouds using our calibration model are shown in Figs. 8 and 9.

3D reconstruction of the image stack shown in Fig. 5 for calibrated and uncalibrated system is shown in Fig. 8. As only points with sufficient reconstruction confidence are shown, the point cloud obtained from the calibrated multi-line scan system is much denser than the uncalibrated case (390 138 vs. 34 971 valid data points, respectively). Note that the influence of the calibration on the result is of course much stronger for a highly uncalibrated system like this than for well-adjusted systems (cf. Fig. 9).

In Fig. 9 3D reconstructions of two Euro cent coins with diameter 19.75 mm and 18.75 mm are shown obtained using our well adjusted multi-line scan system equipped with an industry-grade high quality optics and transport stage. Comparison between system with and without calibration shows clear superiority of the calibrated case. The 3D model from our calibrated setup not only contains much more valid measurements (775 791 vs. 222 415), but also does not show any signs of lens distortions or other artifacts that are clearly visible in the uncalibrated point cloud. Note that the difference between these two 3D models can be as much as 0.5 mm after their mutual registration. For 3D reconstruction in the uncalibrated case we have used known assumed camera and lens parameters. The transport increment T_{step} for the given setup was $13.8 \mu m$, which corresponds with the z -resolution of $80.4 \mu m$.

Conclusions and outlook

Our contribution presents two novelties: First, we propose a new geometric calibration procedure and the implementation details for multi-line scan systems. An accurate calibration method is a prerequisite for using the multi-line scan camera as an optical 3D measurement device and improves 3D reconstruction signif-

icantly. We propose doing so with the help of a projection to a virtual sensor plane in combination with a subsampling scheme. Secondly, we introduce a high precision dot pattern calibration target fitted with the special 3-dot central element. As the target is made of out-of-the-shelf components, it can be adapted to calibrate high magnification lenses. An accompanying detection algorithm improves detection rate, stability and speed. In the future, we would like to substitute the area-scan calibration preceding the multi-linescan calibration with a method that does not require switching the modes of the camera as well as experimenting with higher magnifications and resolutions in all directions.

References

- [1] Doris Antensteiner, Svorad Štolc, Kristian Valentín, Bernhard Blaschitz, Reinhold Huber-Mörk, and Thomas Pock, High-precision 3D sensing with hybrid light field & photometric stereo approach in multi-line scan framework, *IS&T Electronic Imaging 9*, (2017)
- [2] Jean-Yves Bouguet. Matlab camera calibration toolbox. Caltech Technical Report, (2000)
- [3] Tianen Chen, Ryosuke Shibasaki and Zongjian Lin. A rigorous laboratory calibration method for interior orientation of an airborne linear push-broom camera, *Photogrammetric Engineering & Remote Sensing*, 73.4 (2007)
- [4] Robert T. Collins, A space-sweep approach to true multi-image matching. *Proceedings to Computer Vision and Pattern Recognition (CVPR)*. (1996)
- [5] Jamil Drareni, Peter Sturm and Sebastien Roy. Plane-Based Calibration for Linear Cameras. *OMNIVIS 2008 - 8th Workshop on Omnidirectional Vision, Camera Networks and Non-classical Cameras*. (2008)
- [6] David Ferstl, Christian Reinbacher, Gernot Riegler, Matthias Rother and Horst Bischof. Learning Depth Calibration of Time-of-Flight Cameras. *British Machine Vision Conference*. DOI: 10.5244/C.29.102 (2015)

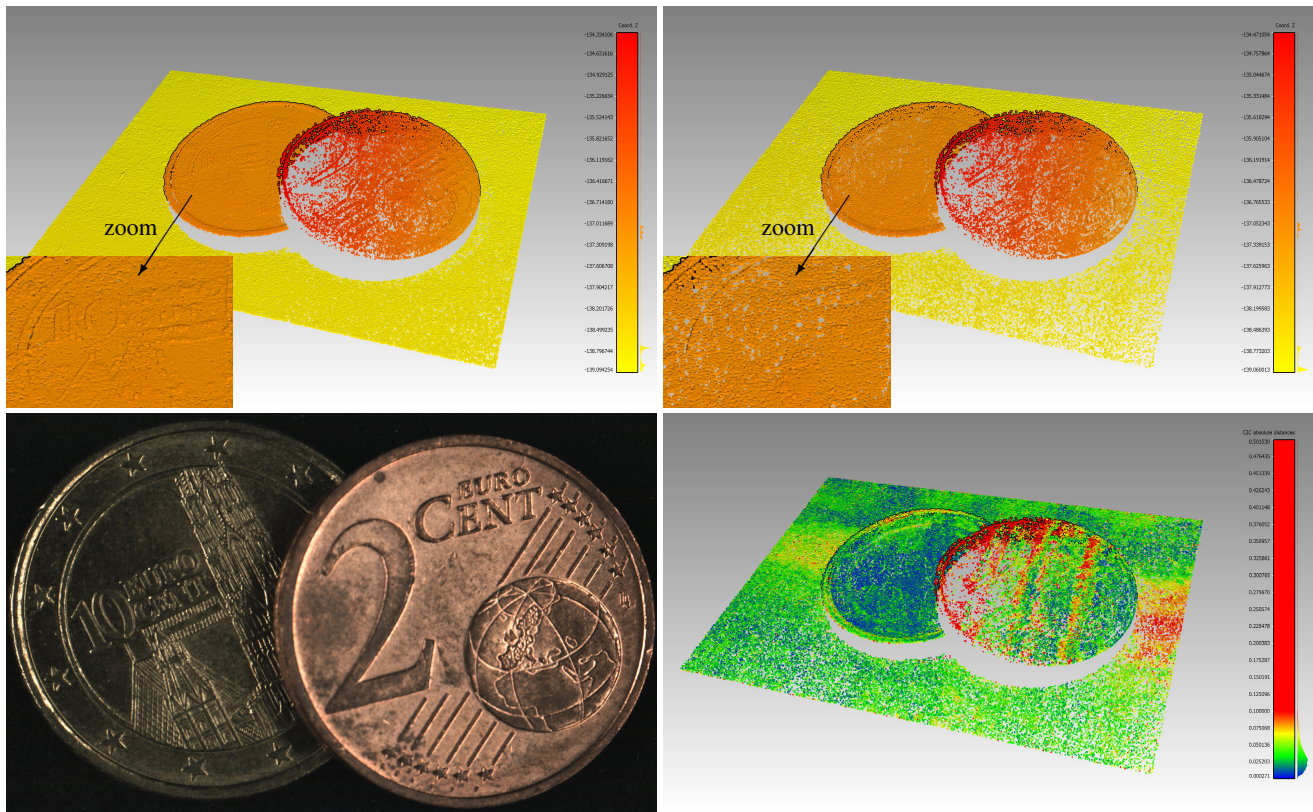


Figure 9: 3D reconstructions of two Euro cent coins (*bottom left*) with diameter 19.75 mm and 18.75 mm obtained using calibrated (*top left*) and uncalibrated (*top right*) system. *Bottom right*: Quantitative comparison between uncalibrated and calibrated point clouds after their mutual registration.

- [7] Rajiv Gupta and Richard I. Hartley, Linear pushbroom cameras, *IEEE Transactions on pattern analysis and machine intelligence* 19,9, pp. 963-975. (1997)
- [8] Heiko Hirschmiller, Frank Scholten and Gerd Hirzinger, Stereo vision based reconstruction of huge urban areas from an airborne pushbroom camera (HRSC), *Lecture notes in computer science* 3663. (2005)
- [9] Radu Horaud, Roger Mohr and Boguslaw Lorecki, On Single-scanline Camera Calibration. *IEEE Transactions on Robotics and Automation*, pp.71-75. (1993)
- [10] Martin Humenberger and Tobias Engelke and Wilfried Kubinger, A census-based stereo vision algorithm using modified semi-global matching and plane fitting to improve matching quality, *Proceedings to Computer Vision and Pattern Recognition Workshops (CVPRW)*. (2010)
- [11] Erik Lilienblum, Ayoub Al-Hamadi and Bernd Michaelis, A coded 3D calibration method for line-scan cameras, *German Conference on Pattern Recognition*. (2013)
- [12] Carlos A. Luna, Manuel Mazo, Jos L. Lazaro, and Juan F. Vazquez, Calibration of line-scan cameras, *IEEE Trans. Instrum. Meas.*, vol. 59, no. 8, pp. 2185-2190. (2010)
- [13] OpenCV Open Source Computer Vision, <http://opencv.org/> (2017)
- [14] Alexander Shekhovtsov and Christian Reinbacher and Gottfried Graber and Thomas Pock. Solving dense image matching in real-time using discrete-continuous optimization. *Proceedings to 21st Computer Vision Winter Workshop (CVWW)*. (2016)
- [15] Svorad Štolc, Daniel Soukup, Branislav Holländer and Reinhold Huber-Mörk, Depth and all-in-focus imaging by a multiline-scan

- light-field camera, *Journal of Electronic Imaging*, 23(5), (2014)
- [16] Qilong Zhang and Robert Pless, Extrinsic calibration of a camera and laser range finder (improves camera calibration), *Proceedings to IEEE/RSJ International Conference on Intelligent Robots and Systems*. (2004)

Author Biography

Dr. Bernhard Blaschitz earned his master's degree in Mathematics from the University of Vienna in 2008 and a PhD degree in Applied Geometry from Technical University of Vienna, Austria in 2014. He joined the AIT Austrian Institute of Technology in 2015 and works as a computer vision scientist at the Center for Vision, Automation & Control.

Dr. Svorad Štolc is a scientist in the Center for Vision, Automation & Control of the AIT Austrian Institute of Technology GmbH, Vienna. He graduated in Computer Science from Comenius University, Bratislava and earned his PhD degree in Bionics and Biomechanics from Technical University of Košice. He is a (co)author of more than 50 peer-reviewed scientific papers and holds a number of patents in machine vision. Since 2016, he coordinates the computational imaging research activities at AIT with the focus on industrial inspection and document security.

Doris Antensteiner is a PhD candidate at the Austrian Institute of Technology (AIT), Vienna in the field of computational imaging and computer vision. She received her masters degree with distinction at the Technical University of Vienna in 2011 in the field of Computer Science. After that she worked at Kapsch, Vienna at the R&D unit Vision and Sensor in the field of computer vision until she joined the AIT in 2015.